

# Vortex Chain States in a Ferromagnet/Superconductor Bilayer

Serkan Erdin

Department of Physics, Northern Illinois University, DeKalb, IL, 60115  
& Advanced Photon Source, Argonne National Laboratory,  
9700 South Cass Avenue, Argonne, IL, 60439

The discrete vortex lattices in a ferromagnet/superconductor bilayer are studied when the ferromagnet has periodic stripe domains with an out-of-plane magnetization. The vortices are assumed to be situated periodically on chains in the stripe domains. Only up to two vortex chains per domain configurations are considered. When the domain period is fixed, the threshold magnetization is calculated at which the transition from the Meissner state to the mixed state occurs. When the domain period is not fixed, the equilibrium domain size and vortex positions are calculated, depending on the domain's magnetization and the domain wall energy. In equilibrium, the vortices in the neighbor domains are half-way shifted, while they are next to each other in the same domain.

PACS numbers:

PACS Number(s): 74.25.Dw, 74.25.Ha, 74.25.Qt, 74.78.-w

## INTRODUCTION

In recent years, heterostructures made of type II superconductors and ferromagnetic pieces have been the focus of studies both experimental and theoretical [1, 2]. In these structures, the magnet and the superconductor are separated by an oxide layer to avoid the proximity effect and spin diffusion that might lead to the suppression of ferromagnetic (FM) and superconducting (SC) order parameters. Therefore, the interaction between the FM textures and the vortex matter in SC pieces is maintained only by the magnetic fields generated by the SC vortices and the magnet. This strong interaction not only gives rich physical effects that are not observed in individual subsystems, but also offers new devices that can be tuned by weak magnetic fields.

One of the realizations of such heterostructures is a ferromagnetic/superconducting bilayer (FSB). In recent years, FSBs have drawn a great deal of attention both experimentally and theoretically. On the experimental side, nonsymmetric current-voltage characteristics on  $\text{La}_{0.66}\text{Sr}_{0.33}\text{MnO}_3/\text{YBa}_2\text{Cu}_3\text{O}_7$  were studied [3]. It has also been reported that stray fields from domain structures of an FM film lead to a significant decrease of the SC critical temperature  $T_c$  in a zero external field, whereas  $T_c$  is enhanced under an applied field [4]. The influence of magnetic domain walls on SC critical temperature was theoretically studied on the basis of the Ginzburg-Landau approach [5]. On the theoretical side, much attention has been paid to the interplay between the vortex matter and the FM layer. Sonin studied the conditions for the penetration of a vortex near a magnetic domain wall [6]. Helseth et al. investigated the pinning of vortices near the magnetic domain walls [7]. Recently, Laiho et al. investigated the vortex structures

in the FSB, when the FM layer has domain structure with out-of-plane magnetization [8]. Two possible vortex structures were shown to occur: vortices with alternating directions corresponding to the direction of the magnetization in FM domain and vortex semiloops connecting the adjacent FM domains.

Earlier Lyuksyutov and Pokrovsky [9, 10] noticed that, in a bilayer consisting of homogeneous SC and FM films with the magnetization normal to the plane, SC vortices occur spontaneously in the ground state, even though the magnet does not generate a magnetic field in the SC film.

In previous work, we presented a theory of such vortex-generation instability and the resulting vortex structures [11]. We showed that, due to this instability, domains with alternating magnetization and vortex directions occur in a FSB. In that study, the domain structures were treated in the continuum regime in which the domain size was much larger than the effective penetration depth,  $\lambda = \lambda_{sc}^2/d_{sc}$ , where the London penetration depth  $\lambda$  is much larger than the thickness of a SC film  $d_{sc}$  [12]. Under the continuum approximation, the energy of stripe phase was found to be minimal. The equilibrium domain size and the equilibrium energy for the stripe structure were found as [11]

$$L_{eq}^{(str)} = \frac{1}{4} \exp\left(\frac{\mu_{dw}}{4\pi^2} C + 1\right); \quad (1)$$

$$U_{eq}^{(str)} = \frac{16\pi^2 A}{4\pi^2} \exp\left(\frac{\mu_{dw}}{4\pi^2} + C - 1\right); \quad (2)$$

where  $\pi = m^2 \mu_v = 0$ ,  $\mu_v = (\frac{2}{0} = 16^2) \ln(\frac{1}{2})$  is the self-energy of a vortex,  $\mu_{dw}$  is the domain wall energy per domain wall length,  $A$  is the domain's area and  $C = 0.577$  is the Euler-Mascheroni constant. If  $\mu_{dw} \ll 4\pi^2$ , the continuum approximation becomes invalid, since  $L_{eq}$  becomes on the order of or less than  $\lambda$  (see Eq.(1)). However, it can be recovered by considering the discrete lattice of vortices instead.

In this paper, the discrete lattice of vortices in the stripe domains is studied through a method that works in both continuum and the discrete regimes. The method we use here is based on London-Maxwell equations and was developed elsewhere [13]. Earlier, its extension to periodic systems for the case of square magnetic dot arrays on a SC film was used [4]. In this work, it is adapted to the discrete vortex lattices in SC/FM bilayers. In doing so, we assumed that vortices and antivortices sit periodically on chains in the alternating domains of magnetization and vorticity. Recently, Karapetrov et al. observed vortex chains in mesoscopic superconductor-normal metal heterostructures by means of scanning tunneling spectroscopy techniques [15]. Vortex chains are also observed in anisotropic high  $T_c$  superconductors (see review [16]). We first studied the vortex lattices in the FSB when the FM domain size is fixed. In this case, we investigated when the vortices appear spontaneously in the FSB, depending on the domain size and the magnetization strength of the domains. We found that one chain per domain configuration appears first, followed by two chains per domain state upon further increase of magnetization at the fixed domain period. Next, we considered the case in which the domain size is not fixed. For this case, the following problems were studied; i) when the domain structures appear spontaneously; ii) how the vortices and the antivortices are positioned on the chains; iii) how the equilibrium domain size changes, depending on the magnetization and the magnetic domain wall energy in the presence of the vortices. In order to solve these problems, we first proposed different configurations of the vortex and the antivortex chains, in which at most two chains per stripe are considered. Next, we calculated their equilibrium energies by means of numerical methods and found the most favorable case among them by minimizing their energies with respect to domain size and vortex positions. Our calculations showed that, in equilibrium structure, vortex chains are halfshifted in the adjacent domain, while they are next to each other in the same domain. The comparison of equilibrium energies of cases with one and two chains per domains shows that, at lower values of magnetization and domain wall energy, the case with two chains is energetically favorable. Additionally, the single-chain case does not win over the ones with two chains per domain in the equilibrium domain structures.

The outline of this paper is as follows: in the following section, the method for the discrete case and its application to configurations with single-vortex chain and double-vortex chains per domain is introduced. The third section is devoted to our results for vortex chain states in the domains with a fixed period. In the fourth section, we present our results on the proposed configurations of single-chain and double-chain cases when they are in the equilibrium domain structures. The last section consists of the conclusions and discussion. In the appendix,

the details of the methods and mathematical tricks in the series calculations are given.

## METHOD

In the continuum approximation, we found that the vortex density increases at closer distances to the magnetic domain walls. Based on this fact and the symmetry of the stripe domain structure, it is reasonable to consider that the vortices and antivortices form periodic structures on straight chains along the  $y$  direction. Even though it is not clear how many chains are associated with each domain, we can still make progress toward understanding discrete vortex lattices. To this end, we propose stripe domain configurations in which vortices are situated periodically on chains. From this point on, the configurations with  $N$  vortex chains per stripe domain are labeled as  $N$  state.

In two of the proposed cases, there is one chain per stripe ( $N = 1$  states), located in the middle of the domain. In this case, two configurations of vortex lattice are possible. First, the vortices and the antivortices in a neighboring domain are alongside one another (see Fig. 1(a)); second, they are shifted by half period  $b=2$  along the  $y$  direction, where  $b$  is the distance between two nearest vortices on the chain (see Fig. 1(b)).

In the other three candidate lattice structures, there are two chains per stripe domain ( $N = 2$  states), at a distance  $a$  from the magnetic domain walls. The possible situations in the two-chain cases are as follows. First, chains in the same domain are shifted by a half period  $b=2$  along the  $y$  direction (see Fig. 1(c)). However, the neighbor vortices and antivortices are next to each other. Second, they are just shifted by a half period  $b=2$  (see Fig. 1(e)). Third, the vortices and the antivortices are simply side by side on the chains (see Fig. 1(f)).

Our next step was to write the energies of these configurations. To this end, we used the energy equations for periodic systems developed elsewhere [14].

$$u_{vv} = \frac{2}{4} \frac{X}{A^2} \frac{F_G^2}{G(1+2G)}; \quad (3)$$

$$u_{mv} = \frac{0}{A} \frac{X}{G} \frac{m_{zG} F_G}{1+2G}; \quad (4)$$

$$u_{mm} = \frac{2}{G} \frac{X}{G} \frac{G^2 \sum_{zG} j_z^2}{1+2G}; \quad (5)$$

In these equations, the vortex configurations differ by their form factors. We can obtain them from  $F_G = \sum_{r_i} n_i e^{iG \cdot r_i}$ , where the  $G$ 's are the reciprocal vectors of the periodic structures, the  $r_i$  are the positions of the vortex centers, and  $n_i$  are the charge of the vortex. In our proposed models,  $G = ((2r+1)\frac{\pi}{L}; 2s\frac{\pi}{b})$  and  $n_i = \pm 1$ .

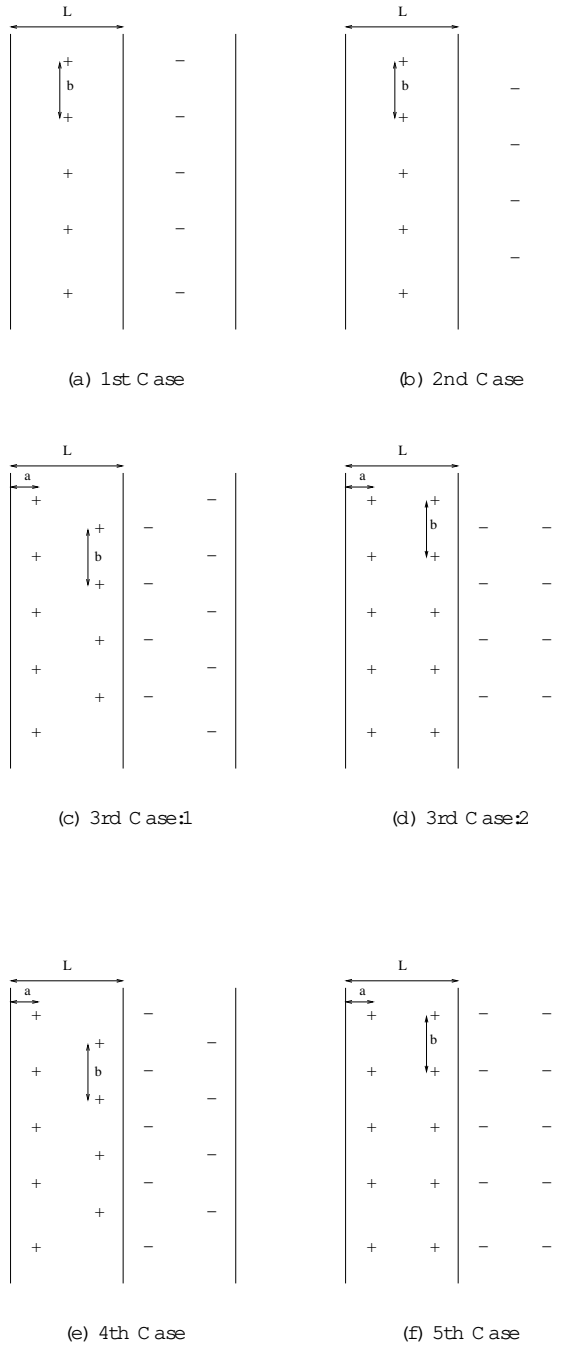


FIG. 1: Proposed configurations for  $N = 1$  and  $N = 2$  states.

Table I gives the form factors of each configuration in the order they are described above.

Note that, in Table I, the form factor for the third configuration also belongs to the case in which the vortex and the antivortex chains are shifted by half period only in the neighbour domains, not in the same domain (see

TABLE I: The form factors of vortices in the proposed configurations.

configuration	$F_G$
1	$i(1)^r$
2	$i(1)^r(1 + (-1)^s)$
3	$2i \sin G_x a (1 + (-1)^s)$
4	$e^{iG_x a} (1)^s e^{-iG_x a}$
5	$2i \sin G_x a$

Fig. 1(d)). Since information about the vortex lattice is carried only by the form factors, there is no need to consider the above-mentioned case separately.

In our calculations, the divergent part of the series must be extracted carefully. We show below a detailed analysis of the series equations for each candidate. We start with the self-interaction energy of the magnetic layer  $U_{mm}$ , since it is the same for each configuration. For the periodic structures, it is given by Eq. (5). Direct substitution of the Fourier coefficient of the stripe phase  $m_{zG} = \frac{2im}{(2r+1)}$  into Eq. (5) gives the self-interaction of the magnetic layer per unit cell as

$$U_{mm} = \frac{8m^2 \chi^2}{L} \sum_{r=0}^{\infty} \frac{1}{\frac{L}{2} + 2r + 1}; \quad (6)$$

where  $\chi^{(0)}(x)$  is the polygamma function of zeroth order [17]. In our numerical calculations, we write the logarithmic term in Eq. (6) as  $\ln(\frac{L}{2}) + \ln(\frac{L}{2})$  and then incorporate the  $4m^2 \ln(\frac{L}{2})$  term in the renormalized  $u_{dw}^{ren}$ . Another energy term with a divergent series is the vortex energy, in general given by Eq. (3). The logarithmic divergence in this term stems from the vortex self-energies. We first split Eq. (3) into two parts as follows:

$$u_{vv} = \frac{u_0}{2L^2 b^2} \sum_G \frac{F_G^2}{G^2} - \frac{F_G^2}{G^2 (1 + 2|G|)}; \quad (7)$$

Note that the area of the unit cell is  $2Lb$ . The first term of the series above contributes to the self-energies of the vortices; whereas, the second term is the vortex-vortex energy and will be left in the series form. For each form factor in Table I, the series in the first term can be transformed to the form of  $\sum_{r=1}^{\infty} \sum_{s=1}^{\infty} \frac{1}{1 + ((2r+1)^2 x^2 + s^2)}$ , where  $x$  is constant, and depends on the form factor. A detailed analysis of such a series is given in the appendix.

The next step is to find the vortex energy and the interaction energy of the magnetization and vortices for each configuration. In the calculation of  $u_{vv}$ , we take the Fourier coefficient of the magnetization to be

$\frac{4im}{(2r+1)} (G_y)$ . The fact that the stripe is infinite along the  $y$  direction results in the additional term  $2 (G_y)$ . However, it does not play any role in the calculation of  $u_{mm}$ . For numerical analysis, these energies must be expressed in terms of dimensionless parameters. To this end, we define dimensionless variables  $\tilde{x} = x/L$ ,  $\tilde{y} = y/L$

and  $u_{dw} = u_{dw}^{ren} = u_0$ . The total energy  $U$  is measured in units of  $u_0 = \frac{2}{\epsilon}$ . In addition, we introduce the dimensionless magnetic energy as  $U_{mm} = u_{mm} = (u_0 = \frac{2}{\epsilon})$ . In terms of these parameters, the energy of the first configuration reads

$$U^{(1)} = \frac{\tilde{x}^2}{4\tilde{b}} \ln \frac{4}{e^c \tilde{x}} + 2f_v^{(1)}(\tilde{x}) \frac{2f_{vv}^{(1)}(\tilde{x}; \tilde{b})}{\tilde{b}} \frac{16m_0}{u_0} f_{mv}^{(1)}(\tilde{x}) + U_{mm} + u_{dw} \tilde{x}; \quad (8)$$

where,

$$\begin{aligned} f_v^{(1)} &= \sum_{r=0}^{\tilde{x}} \frac{\coth((2r+1)\frac{\tilde{b}}{2}) - 1}{2r+1}; \\ f_{vv}^{(1)} &= \sum_{r;s=1}^{\tilde{x}} \frac{1}{(2r+1)^2 + \frac{4s^2}{\tilde{b}^2}} (1 + 2 \sim (2r+1)^2 + \frac{4s^2}{\tilde{b}^2}); \\ f_{mv}^{(1)} &= \sum_{r=0}^{\tilde{x}} \frac{(1)^r}{(2r+1)(1 + 2 \sim (2r+1))}; \end{aligned} \quad (9)$$

The form factor for the second configuration survives only for even values of  $s$ . Then, the dimensionless energy of the second configuration is found to be

$$U^{(2)} = \frac{\tilde{x}^2}{2\tilde{b}} \ln \frac{4}{e^c \tilde{x}} + 2f_v^{(2)}(\tilde{x}) \frac{4f_{vv}^{(2)}(\tilde{x}; \tilde{b})}{\tilde{b}} \frac{16m_0}{u_0} f_{mv}^{(2)}(\tilde{x}) + U_{mm} + u_{dw} \tilde{x}; \quad (10)$$

where  $f_{mv}^{(2)} = f_{mv}^{(1)}$  and,

$$\begin{aligned} f_v^{(2)} &= \sum_{r=0}^{\tilde{x}} \frac{\coth((2r+1)\frac{\tilde{b}}{4}) - 1}{2r+1}; \\ f_{vv}^{(2)} &= \sum_{r;s=1}^{\tilde{x}} \frac{1}{(2r+1)^2 + \frac{16s^2}{\tilde{b}^2}} (1 + 2 \sim (2r+1)^2 + \frac{16s^2}{\tilde{b}^2}); \end{aligned} \quad (11)$$

In the third configuration, as in the second configuration, only even values of  $s$  contribute to the energy. In the first two configurations, the square of their form factors enter the vortex energy as a constant. However, in this case, the square of the sine function appears. In the

appendix, the calculation of the series in the presence of such functions is shown. Introducing the dimensionless parameter  $a = a/L$ , the energy functional of the third configuration becomes

$$U^{(3)} = \frac{\tilde{x}^2}{\tilde{b}} \ln \frac{4}{e^c \tilde{x}} \ln(\cot(a)) + 4f_v^{(3)}(\tilde{x}; a) \frac{8}{\tilde{b}} f_{vv}^{(3)}(\tilde{x}; a; \tilde{b}) \frac{16m_0}{u_0} f_{mv}^{(3)}(\tilde{x}; a)$$

$$+ \mathcal{U}_{m m} + \mathcal{U}_{d w} \sim ; \quad (12)$$

where,

$$\begin{aligned} f_v^{(3)} &= \sum_{r=0}^{\infty} \frac{\coth((2r+1)\frac{b}{4}) - 1}{2r+1} \sin^2((2r+1) a); \\ f_{vv}^{(3)} &= \sum_{r;s=1}^{\infty} \frac{\sin^2((2r+1) a)}{(2r+1)^2 + \frac{16s^2}{b^2} (1+2 \sim (2r+1)^2 + \frac{16s^2}{b^2})}; \\ f_{mv}^{(3)} &= \sum_{r=0}^{\infty} \frac{\sin((2r+1) a)}{(2r+1)(1+2 \sim (2r+1))}; \end{aligned} \quad (13)$$

In the fourth configuration, the square of the form factor is:

$$\mathcal{F}_G^2 = 2 \sum_{r=0}^{\infty} (1)^s \cos((2r+1) a). \text{ Even and odd values}$$

of  $s$  give different contributions. Then, we can calculate the vortex energy for even  $s$  and odd  $s$  separately.

Employing similar techniques, we find

$$\mathcal{U}^{(4)} = \frac{\sim 2}{2b} \ln \frac{4}{e^c \sim} + 2f_v^{(4)}(\sim; a) + \frac{4}{b} f_{vv}^{(4)}(\sim; a; b) + \frac{16m}{\mu_0} f_{mv}^{(4)}(\sim; a) + \mathcal{U}_{m m} + \mathcal{U}_{d w} \sim ; \quad (14)$$

where  $f_{mv}^{(4)} = f_{mv}^{(3)}$  and,

$$\begin{aligned} f_v^{(4)} &= \sum_{r=0}^{\infty} \frac{\coth((2r+1)\frac{b}{4}) - 1}{2r+1} \sin^2((2r+1) a) + \sum_{r=0}^{\infty} \frac{\tanh((2r+1)\frac{b}{4}) - 1}{2r+1} \cos^2((2r+1) a); \\ f_{vv}^{(4)} &= \sum_{r;s=1}^{\infty} \frac{\sin^2((2r+1) a)}{(2r+1)^2 + \frac{16s^2}{b^2} (1+2 \sim (2r+1)^2 + \frac{16s^2}{b^2})} \\ &+ \sum_{r;s=1}^{\infty} \frac{\cos^2((2r+1) a)}{(2r+1)^2 + \frac{4(2s+1)^2}{b^2} (1+2 \sim (2r+1)^2 + \frac{4(2s+1)^2}{b^2})}; \end{aligned} \quad (15)$$

The form factor for the fifth case resembles that of the third case with an exception. That is, in the third case, only even values of  $s$  are taken into account, while

all integers contribute to the sum over  $s$  in the fifth case. Keeping this in mind, obtaining the dimensionless energy for the last case is straightforward:

$$\begin{aligned} \mathcal{U}^{(5)} &= \frac{\sim 2}{2b} \ln \frac{4}{e^c \sim} + \ln(\cot(a)) + 4f_v^{(5)}(\sim; a) + \frac{4}{b} f_{vv}^{(5)}(\sim; a; b) + \frac{16m}{\mu_0} f_{mv}^{(5)}(\sim; a) \\ &+ \mathcal{U}_{m m} + \mathcal{U}_{d w} \sim ; \end{aligned} \quad (16)$$

where  $f_{mv}^{(5)} = f_{mv}^{(3)}$  and,

$$\begin{aligned} f_v^{(5)} &= \sum_{r=0}^{\infty} \frac{\coth((2r+1)\frac{b}{2}) - 1}{2r+1} \sin^2((2r+1) a); \\ f_{vv}^{(5)} &= \sum_{r;s=1}^{\infty} \frac{\sin^2((2r+1) a)}{(2r+1)^2 + \frac{4s^2}{b^2} (1+2 \sim (2r+1)^2 + \frac{4s^2}{b^2})}; \end{aligned} \quad (17)$$

## COMPUTATIONAL METHODOLOGY

The series in  $f_v^{(i)}$  converges very fast when  $r_{m\ ax} > 200$ , while the series in  $f_{vv}^{(i)}$  converges rather slowly. When  $r_{m\ ax} > 4000$  and  $s_{m\ ax} > 4000$ , the results do not change up to the 6th decimal point in the energy, where  $i$  labels the particular domain configuration. To make sure of this accuracy in the calculations, we take  $r_{m\ ax} = 600$  for  $f_v^{(i)}$ ,  $r_{m\ ax} = 5000$  for  $f_{mv}^{(i)}$ , and  $r_{m\ ax} = 5000$  and  $s_{m\ ax} = 5000$  for  $f_{vv}^{(i)}$  in Eqs.(8, 10, 12, 14, 16). In addition, the respective error deviations for  $a=L, b=L$  and  $a=L$  in numerical calculations are 0:005, 0:0005 and 0:0125. In the numerical computations of Eqs.(8, 10, 12, 14, 16), we take  $\ln(4/\epsilon) = 5.57$ .

## THE VORTEX CHAIN STATES IN DOMAINS WITH FIXED PERIOD

Here, the conditions for the transition from the Meissner state to the mixed state when the vortices first spontaneously appear, are determined. As described in the second section, the total energy of the bilayer consists of the self-vortex energies  $u_v$ , vortex-vortex interaction  $u_{vv}$ , vortex-magnetization interaction  $u_{mv}$ , the self-interaction of magnetic domains  $u_{mm}$  and the domain wall energy  $u_{dw}$ . The last two terms are necessary only to determine the equilibrium domain size. Therefore, they are irrelevant when the domain period is fixed, and they will be ignored in the further calculations to determine when the Meissner state-mixed state transition occurs. Now, we call the total energy of interest, the effective energy to avoid any confusion in the rest of the paper. The effective energy has the form  $U = u_v + u_{vv} + u_{mv}$ . The detailed versions of these terms for each proposed configuration were described in the second section. Next, we calculate the equilibrium effective energies of each configuration for fixed values of  $m_0 = m_0$  and  $a=L$ . In doing so, the effective energies are minimized with respect to the vortex positions. The necessary condition for the vortices to appear spontaneously is  $U_{eff} < 0$ . Our numerical calculations show that the configurations with a single vortex chain per domain ( $N = 1$  state) appear first in the mixed state. Note that there are two configurations for the  $N = 1$  state. In our calculations, it turns out that they are indistinguishable when the transition occurs. Next, the values of  $m_0 = m_0$  that make  $U_{eff}^{N=1}$  zero for various values of the domain period, are calculated. Thus, the curve that separates the Meissner state and  $N = 1$  state is obtained (see the bottom curve in Fig. 2). The fit of our numerical data yields an equation for this curve as:  $m_0 = m_0 = 2.75(a=L)^{0.67}$ . Earlier, Laiho et al. [8] calculated critical magnetizations for two cases: penetration of a vortex from a domain center and penetration of a vortex semiloop from a domain wall in a

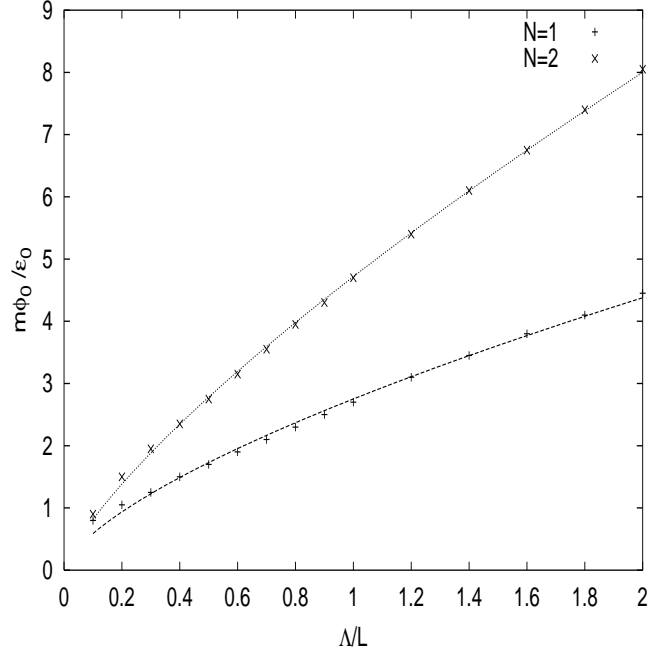


FIG. 2: Phase diagram showing transition from the Meissner state to the mixed state, depending on  $m_0 = m_0$  and  $a=L$ . The region below the  $N = 1$  curve corresponds to the Meissner state, while  $N = 1$  state exists in the area between the  $N = 1$  and  $N = 2$  curves. The  $N = 2$  state becomes energetically favorable above the  $N = 2$  curve.

FSB, in which both FM and SC layers are thick. For the former case, they found that the critical magnetization decreases with the increase of domain period. This result is in full agreement with ours. When vortices appear first in FSB, the inter-vortex distance  $b$  grows. With further increase of the magnetization, they get close. Note that our results here do not give any information regarding which configuration of  $N = 1$  becomes favored in the mixed state.

We also studied the transition from the  $N = 1$  state to the  $N = 2$  state. The necessary conditions for this transition are  $U_{eff}^{N=2} < U_{eff}^{N=1}$  and  $U_{eff}^{N=2} < 0$ . Our calculations show that the third configuration wins over the fourth and fifth configurations for the  $N = 2$  state. Note that the effective energy of the third configuration corresponds to two cases that have the same structure factor. Which one is likely to win over is discussed in the next section. Following steps similar to those described above, we obtained the curve  $m_0 = m_0 = 4.72(a=L)^{0.76}$  (see the top curve in Fig. 2). Furthermore, when the  $N = 2$  state wins over the  $N = 1$  state,  $b$  and  $a$  are on the order of a few  $\xi$ . The increasing magnetization leads to a significant decrease of these parameters.

THE VORTEX CHAIN STATES IN THE  
EQUILIBRIUM DOMAIN STRUCTURES

Here, we first investigated when the proposed cases become energetically favorable. To this end, we checked when the equilibrium energies of the cases first become negative. To do so, the energies of the proposed cases Eqs.(8,10,12,14,16) for different values of  $m_0 = \mu_0$  and  $\mu_{dw}$  were calculated by minimizing their energies with respect to the domain size and the vortex positions. From this procedure, one can determine which case's equilibrium energy becomes negative first and then calculate the corresponding values of  $m_0 = \mu_0$  and  $\mu_{dw}$ . Our calculations show that the equilibrium energy of the third case associated with the  $N = 2$  state turns to negative first. When the  $N = 2$  state first appears, the domain size and inter-vortex distance on the same chain are on the order of a few tens of  $\lambda$ . This suggests that, in equilibrium, vortex chain states appear near the domain walls. It is expected that vortex chain states proliferate with further increase of the magnetization. This result is consistent

with our previous work in which the vortex density in the continuum approximation increases substantially near the magnetic domain walls. In Fig. 3, the phase diagram for the  $N = 2$  state is depicted. The dots in the figure are obtained from our simulations. The curve is fitted to the simulation data. The fit gives the curve  $m_0 = \mu_0 = 1.37\mu_{dw}^{0.34}$ . Below the curve, there is not any stable configuration, while, above the curve, the third configuration corresponding to  $N = 2$  state exists.

Nonetheless, this information is not enough for us to understand the equilibrium structure, since  $\mathcal{U}^{(3)}$  corresponds to two different configurations with the same structure factor. At this point, further analysis is needed to determine which configuration is more likely. To this end, we calculated the minimal energy of each case in both continuum and discrete regimes, depending on  $m_0 = \mu_0$  at fixed  $\mu_{dw}$ . The equilibrium energies for these cases in discrete and continuum regimes are given in Table II. Note that small and large values of  $m_0 = \mu_0$  for each  $\mu_{dw}$  correspond to continuum and discrete regimes, respectively.

TABLE II: Equilibrium energies for proposed configurations. Two columns on the left are input.

$\mu_{dw}$	$m_0 = \mu_0$	$\mathcal{U}_1$	$\mathcal{U}_2$	$\mathcal{U}_3$	$\mathcal{U}_4$	$\mathcal{U}_5$
0.01	5	-2.58454176	-2.58455668	-3.36407195	-3.36404625	-3.36404615
0.01	20	-65.98296440	-65.98296500	-89.20105311	-89.20030961	-89.20030943
0.1	5	-2.54211623	-2.54211637	-3.33057991	-3.33054828	-3.32949063
0.1	20	-65.87136440	-65.87136500	-89.10475311	-89.10310961	-89.10310943
1	5	-2.16635495	-2.16637343	-3.01972350	-3.01972355	-3.01972347
1	20	-64.78187766	-64.781878054	-88.15826391	-88.15826394	-88.15826367
10	5	-0.35644861	-0.35667498	-1.21258278	-1.21232397	-1.21232396
10	25	-95.00241100	-95.00247780	-134.28090345	-134.27589780	-134.27589769

In our numerical calculations, we find that all proposed configurations are stable in both the discrete and continuum regimes, indicating that our method works well in both regimes. As in the previous section, the third case associated with the  $N = 2$  state wins over the other two chains-per-domain configurations. As said before, the energy of the third case corresponds to two configurations. Which configuration is more likely to appear in equilibrium can be figured out from simple physical considerations. Namely, in FSB, the equilibrium structure is determined by the competition between vortex-vortex and vortex-magnetization interactions. The former favors vortices and antivortices in the neighbor domains to line up in a transverse direction (perpendicular to the magnetic domain wall), whereas the latter prefers vortices and antivortices to be shifted so that gain in energy

is maximized. When vortices are next to each other on either side of the magnetic domain wall, the magnetic fields they produce cancel out each other. From the numerical results, it is obvious that vortex-magnetization interaction wins the competition and results in half-way shifting of vortices, if one compares the energies of the 1st and 2nd cases. Then, vortex-magnetization interaction is the dominant factor. By the same token, one can understand what is going on in double-vortex chain configurations. For instance, in the fifth configuration, energy gain due to vortex-magnetization interaction is diminished, since all the vortices are side by side. This explains why the equilibrium energy of the fifth configuration is higher than those of the third and fourth cases. In the fourth configuration, the vortices and antivortices in the neighbor domains are shifted half-way, so that this

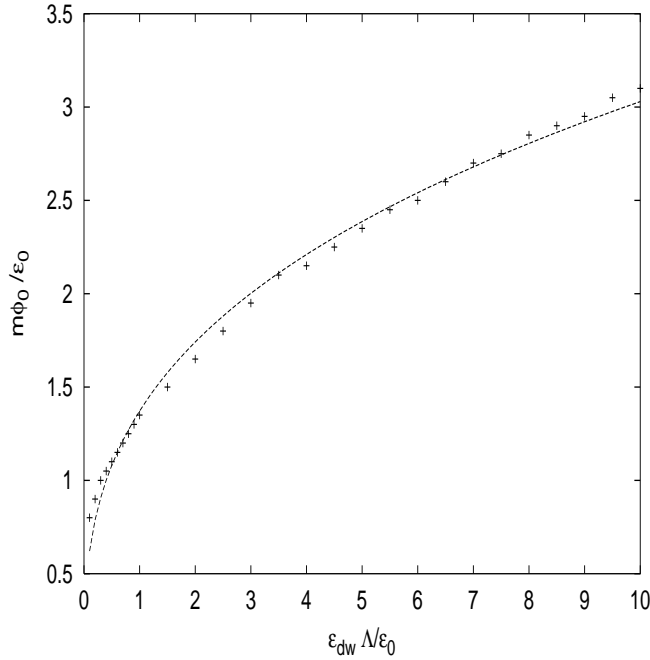


FIG . 3: The phase diagram for the third case  $N = 2$  state. The  $N = 2$  state becomes stable in the region above the curve.

configuration must be preferred over the one in which they sit side by side in the neighbor domains according to the above arguments. However, an alternative configuration for the third case has two chains shifted halfway in the neighbor domains instead of one chain as in the fourth case. Therefore, one might expect the gain to be even more than that in the fourth configuration. Another interesting result is that the system does not favor the  $N = 1$  state at all. Actually, this does not surprise us, since, in the continuum approximation, we found that the vortex density increases near the magnetic domain walls. This fact already suggests that the system favors vortex chains being near the magnetic domain walls rather than a single chain in the middle of the domain.

In numerical calculations, equilibrium domain size  $L=$ , vortex-vortex distances on the same chain  $b=$  and vortex-magnetic domain wall distances  $a=$  are also calculated. Results for the third configuration at various values of  $m_0=\mu_0$  and  $\mu_{dw}$  are depicted in Figs. 4, 5, 6. Results for other configurations are not shown here, since they look quite similar. At fixed  $\mu_{dw}$ , the further increase of  $m_0=\mu_0$  shrinks the domain width, while a higher domain wall energy favors a larger domain width at fixed  $m_0=\mu_0$ , as in usual ferromagnets. That is to say, ferromagnet favors narrower domains to minimize the demagnetization energy, whereas domain wall energy makes domains wider. The competition between these two energies determines the domain size. Here, the pa-

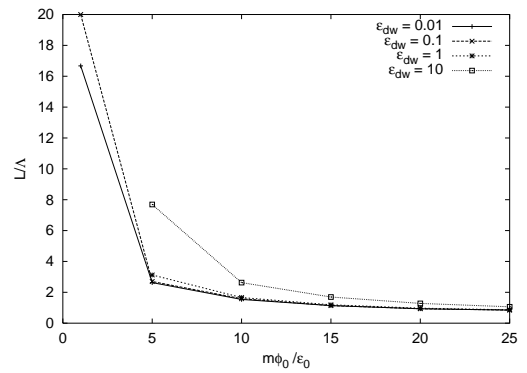


FIG . 4:  $L=$  versus  $m_0=\mu_0$  for the third configuration.

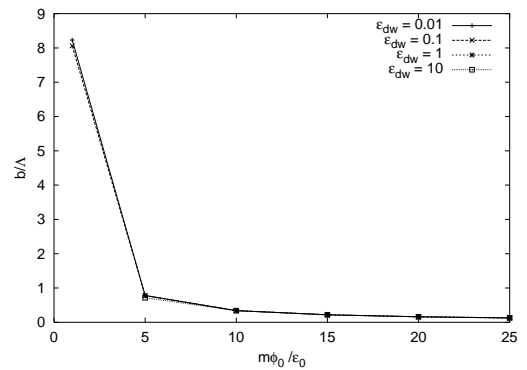


FIG . 5:  $b=$  versus  $m_0=\mu_0$  for the third configuration.

rameter  $m_0=\mu_0$  plays the role of demagnetization energy. Domain wall energy does not affect the distance between the vortices located on the same chain. However, at larger values of  $m_0=\mu_0$ , the vortices on the same chain get closer. This implies that the unit cell area shrinks, and consequently vortex density per area increases.

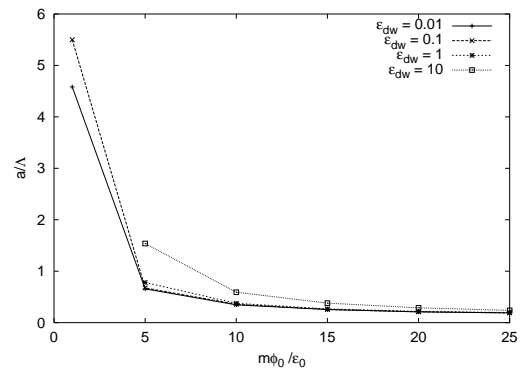


FIG . 6:  $a=$  versus  $m_0=\mu_0$  for the third configuration.



## CONCLUSIONS

In this article, we reported our results on the lattices of discrete vortices in stripe domains in FSB using a method based on Maxwell-London equations. If  $\mu_{dw} = 4\pi^2$ , the continuum approximation becomes invalid. Instead, we considered the discrete lattice of vortices in which the vortices were considered to be situated on chains directed along the stripes. We analyzed the vortex configurations up to two vortex chains in two cases: first, we took the domain period to be fixed, second, the domain period was not fixed. In the former case, we calculated the threshold magnetization at which the transition from the Meissner and mixed state occurred. We showed that configurations corresponding to the  $N = 1$  state appeared first in the mixed state. With a further increase of magnetization, the  $N = 2$  state becomes more favorable. The critical magnetization for transition from the  $N = 1$  to the  $N = 2$  state was also calculated. In the second case, depending on the magnetization and the magnetic domain wall energy, the equilibrium energy, the positions of the vortices and the equilibrium domain size were calculated. According to our calculations, in equilibrium, vortices on the either side of the magnetic domain walls are not side by side on the chains; instead, they are shifted by a half period along the stripe, while they are side by side in the same domain. The threshold magnetization as a function of domain wall energy for this case was calculated.

In numerical calculations, we also found that the vortex lattice is stable for  $\mu_{dw} > 4\pi^2$ . At this point, the domain size is noticeably larger than the effective penetration depth, so the continuum approximation is valid. Therefore, we expect that the domain nucleation starts in the continuum regime. This problem is left for the future research. At constant  $\mu_{dw}$ , with increasing  $m_0 = \mu_v$ , the equilibrium size of the domain decreases. In addition, the vortices on the chain get closer to each other. These results agree with those obtained in the continuum approximation. As  $\mu_{dw} = 4\pi^2$  increases, we expect that new vortex chains develop within the domains. We leave the detailed analysis of this problem to another publication. In concluding, we believe that confined geometries, such as domains in FSB, lead to novel vortex structures, which might be experimentally investigated by means of scanning tunnelling spectroscopy.

## ACKNOWLEDGMENTS

The most of this work was done during my stay at the University of Minnesota and was partially supported by the U.S. Department of Energy, Office of Science, under

Contract No. W-31-109-ENG-38.

## CALCULATIONS OF SERIES

In this appendix, the detailed analysis of the series is given. First, the series in the energy calculations of the periodic systems are analyzed; second, the detailed calculation of the vortex density is shown. The series we encounter in the energy calculations fall into two categories. In the first category, we sum over one variable. The series in this category are in the form of  $\sum_{r=1}^{\infty} \frac{1}{r}$ . Employing the Euler-Maclaurin summation formula [18], the summation is found with logarithmic accuracy as

$$\sum_{r=1}^{\infty} \frac{1}{r} = \ln r_{max} + C; \quad (A.18)$$

where  $C = 0.577$  is the Euler-Mascheroni constant. If the summation is performed over only odd integers, we can still transform our series to Eq. (A.18). Namely,

$$\begin{aligned} \sum_{r=0}^{\infty} \frac{1}{2r+1} &= \sum_{r=1}^{2r_{max}+1} \frac{1}{r} - \sum_{r=1}^{r_{max}=2} \frac{1}{r}; \\ &= \ln(2r_{max}+1) + C - \ln\left(\frac{r_{max}}{2}\right) - \frac{C}{2}; \\ &= \frac{1}{2}(\ln r_{max} + C + 2\ln 2); \end{aligned} \quad (A.19)$$

The other double series of interest here is in the form of

$$I(x) = \sum_{r=1}^{\infty} \sum_{s=1}^{\infty} \frac{1}{x^2 r^2 + s^2}; \quad (A.20)$$

where  $x$  is an arbitrary constant. Although Eq. (A.20) is logarithmically divergent, the sum over one of the variables can be done easily. To this end, we perform the sum over  $s$  first. In doing so, Eq. (A.20) becomes  $(2-x) \sum_{r=1}^{\infty} \coth(xr) = r$  [19]. This series is logarithmically divergent. In order to get the logarithmic term, we add and subtract  $1=r$ . Using the result in Eq. (A.18), finally we get

$$I(x) = \frac{2}{x} \sum_{r=1}^{\infty} \frac{\coth(xr)}{r} + \ln r_{max} + C; \quad (A.21)$$

Employing the same techniques, we give the results of the different versions of Eq. (A.20) below:

$$\sum_{r=1}^{\infty} \sum_{s=1}^{\infty} \frac{1}{x^2 (2r+1)^2 + s^2} = \frac{2}{x} \sum_{r=0}^{\infty} \frac{\coth((2r+1)x) - 1}{2r+1} + \frac{\ln r_{m \max}}{2} + \frac{C}{2}; \quad (\text{A } 22)$$

$$\sum_{r=1}^{\infty} \sum_{s=1}^{\infty} \frac{1}{x^2 (2r+1)^2 + (2s+1)^2} = \frac{1}{x} \sum_{r=0}^{\infty} \frac{\tanh((2r+1)\frac{x}{2}) - 1}{2r+1} + \frac{\ln r_{m \max}}{2} + \frac{C}{2}; \quad (\text{A } 23)$$

In Eqs.(A 22) and (A 23), we use  $\sum_{s=0}^{\infty} \frac{1}{(y^2 + (2s+1)^2)} = \frac{1}{2y} \tanh(\frac{y}{2}) = \frac{1}{4y}$ . In the presence of  $\sin^2(2r+1)y$  or  $\cos^2(2r+1)y$ , the series can be calculated in a

similar way, using  $\sin^2(2r+1)y = (1 - \cos(2(2r+1)y))/2$  or  $\cos^2(2r+1)y = (1 + \cos(2(2r+1)y))/2$ . For example,

$$\sum_{r=1}^{\infty} \sum_{s=1}^{\infty} \frac{\sin^2(2r+1)y}{(x^2 (2r+1)^2 + s^2)} = \frac{2}{x} \sum_{r=0}^{\infty} \frac{\sin^2(2r+1)y (\coth((2r+1)x) - 1)}{2r+1} + \frac{\ln r_{m \max}}{4} + \frac{\ln |\text{jcot}(y/2)|}{4} + \frac{C}{4}; \quad (\text{A } 24)$$

$$\sum_{r=1}^{\infty} \sum_{s=1}^{\infty} \frac{\cos^2(2r+1)y}{(x^2 (2r+1)^2 + s^2)} = \frac{2}{x} \sum_{r=0}^{\infty} \frac{\sin^2(2r+1)y (\coth((2r+1)x) - 1)}{2r+1} + \frac{\ln r_{m \max}}{4} + \frac{\ln |\text{jcot}(y/2)|}{4} + \frac{C}{4}; \quad (\text{A } 25)$$

We use

$$\sum_{r=0}^{\infty} \frac{\cos((2r+1)x)}{2r+1} = \frac{\ln |\text{jcot}(x/2)|}{2}. \quad (\text{A } 26)$$

- [1] I.F. Lyuksyutov and V.L. Pokrovsky, *Adv. Phys.* 54, 67 (2005).
- [2] S. Erdin, *Frontiers in Superconducting Materials*, edited by A. Narlikar, (Springer-Verlag, Berlin, 2005), pp. 425-458.
- [3] N. Toubou, P. Bernstein, J.F. Hamet, Ch. Simon et al., *Appl. Phys. Lett.* 85, 1742 (2004).
- [4] M. Lange, M.J. Van Bael and V.V. Moshchalkov, *Phys. Rev. B* 68, 174522 (2003).
- [5] A. Yu. Aladyshkin, A.I. Buzdin, A.A. Fraeman, A.S. Melnikov et al., *Phys. Rev. B* 68, 184508 (2003).
- [6] E.B. Sonin, *Pis'ma Zh. Tekh. Fiz.* 14, 1640 (1988) [*Sov. Tech. Phys. Lett.* 14, 714 (1988)].
- [7] L.E. Helseth, P.E. Goa, H. Hauglin, M. Baziljevich, and T.H. Johansen, *Phys. Rev. B* 65, 132514 (2002).
- [8] R. Laiho, E. Lahderanta, E.B. Sonin and K.B. Traito, *Phys. Rev. B* 67, 144522 (2003).

- [9] I.F. Lyuksyutov and V.L. Pokrovsky, cond-mat/9903312 (unpublished).
- [10] I.F. Lyuksyutov and V.L. Pokrovsky, *Modern Phys. Lett. B* 14, 409 (2000).
- [11] S. Erdin, I.F. Lyuksyutov, V.L. Pokrovsky and V.M. Vinokur, *Phys. Rev. Lett.* 88, 017001 (2002).
- [12] A.A. Abrikosov, *Introduction to the Theory of Metals* (North Holland, 1986).
- [13] S. Erdin, A.M. Kayali, I.F. Lyuksyutov and V.L. Pokrovsky, *Phys. Rev. B* 66, 014414 (2002).
- [14] S. Erdin, *Physica C* 391, 140 (2003).
- [15] G. Karapetrov, J. Fedor, M. Iavarone, D. Rosenmann and W.K. Kwok, *Phys. Rev. Lett.* 95, 167002 (2005).
- [16] S.J. Bending and J.W. Dodgson, *J. Phys.: Condens. Matter* 17, R955 (2005).
- [17] M. Abramowitz and I.A. Stegun, *Handbook of Mathematical Functions*, (Dover Publications, New York, 1970).
- [18] G.B. Arfken and H.J. Weber, *Mathematical Methods for Physicists*, (Academic Press, Orlando, 2000), 5th ed.

[19] E. R. Hansen, *A Table of Series and Products*, (Prentice-Hall, Englewood Cliffs, 1975).